Monacelli, L., Errea, I., Calandra, M. *et al.* Black metal hydrogen above 360 GPa driven by proton quantum fluctuations. *Nat. Phys.* (2020).

https://doi.org/10.1038/s41567-020-1009-3

Black metal hydrogen above 360 GPa driven by proton quantum fluctuations

Lorenzo Monacelli,[1] Ion Errea,[2] Matteo Calandra,[3] and Francesco Mauri[1]

Hydrogen metallization under stable conditions is a major quest for realizing the first room temperature superconductor. Recent low-temperature experiments[1–3] report different metallization pressures, varying from 360GPa to 490GPa. In this work, we simulate structural properties, vibrational Raman, IR and optical spectra of hydrogen phase III accounting for proton quantum effects. We demonstrate that nuclear quantum fluctuations downshift the vibron frequencies by 25%, introduce a broad line-shape in the Raman spectra, and reduce the optical gap by 3eV. We show that hydrogen metallization occurs at 380GPa in phase III due to band overlap, in good agreement with transport data[2]. Our simulations predict this state is a black metal - transparent in the IR - so that the shiny metal observed at 490GPa[1] is not phase III. We predict the conductivity onset and the optical gap will substantially increase if hydrogen is replaced by deuterium, underlining that metallization is driven by quantum fluctuations and is thus isotope dependent. We show how hydrogen acquires conductivity and brightness at different pressures, explaining the apparent contradictions in existing experimental scenarios[1–3].

Solid hydrogen at high pressures exhibits a very rich phase diagram with the presence of five different insulating molecular phases, labeled from I to V[4–6], before undergoing a transition into the long-sought atomic metallic state proposed by Wigner and Huntington[7], expected to be a room temperature superconductor[8]. The structural characterization of these phases is challenging since both neutron and X-ray scattering require sample sizes compatible with a pressure lower than 250 GPa[9]. The experimental structural information must be inferred indirectly from vibrational spectroscopy (Raman and IR) and/or optical measurements (transmittance and reflectivity). The experimental difficulties in collecting data and the different probes used have led to apparently contradicting results about the metallization of hydrogen at low temperatures in the solid-state as shown in **Figure** 1. Optical reflectivity measurements suggest metallization of hydrogen in an atomic state at 495 GPa from an unidentified opaque phase[1], electrical measurements observe semimetallic behavior in phase III above 360 GPa[2], while infrared transmission experiments suggest that hydrogen metallizes from phase III after a first-order transition to a metallic phase at 420 GPa[3].

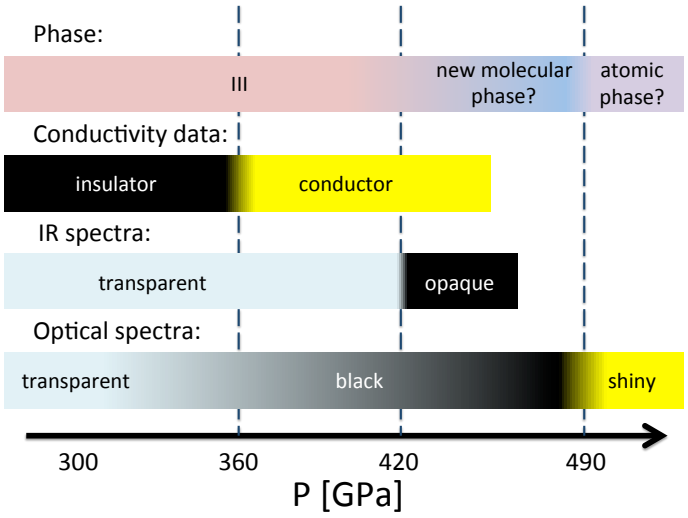

Figure 1. Sketch of the physical properties of low-temperature hydrogen. Optical data and reflectivity measurements[1] argue that hydrogen is black above 320 GPa and seem to indicate it is shiny at 490 GPa. Conductivity measurements[2] show that phase III is a conductor above 360 GPa. IR absorption data[3] show a transparency window at low frequency until 420 GPa, where the transmission abruptly drops to zero. This is a qualitative sketch, as there are mismatches on the pressure calibration between different experiments[3] and the results are highly debated[10].

Numerical *ab initio* simulations play consequently a crucial role in understanding the structures that form the phase diagram of hydrogen. *Ab initio* structural searches successfully elucidated the crystalline morphology of phase II[11] and provided good candidates for phases III[12], IV[13], and V[14]. However, different theoretical approximations yield to distinct low-energy structures, and, thus, a strong debate on the correct identification of the phases is ongoing[15]. All structure searches performed so far on hydrogen assume that nuclei are classical particles. The Born-Oppenheimer energy landscape is explored looking for the global minimum of the energy. However, as hydrogen is the lightest element, its nucleus is subject to huge quantum fluctuations that can largely affect structural properties. For instance, nuclear quantum effects have been shown to completely reshape the energy landscape in the hydrogen-rich H_3S[16] and LaH_{10}[17] compounds as well as in metallic hydrogen[18], invalidating the phase-diagram obtained with classical simulations. Only recently struc-

[1] Department of Physics, University "Sapienza", Rome, Italy
[2] Fisika Aplikatua 1 Saila, Gipuzkoako Ingeniaritza Eskola, University of the Basque Country (UPV/EHU), Europa Plaza 1, 20018, Donostia/San Sebastián, Spain;
Centro de Física de Materiales (CSIC-UPV/EHU), Manuel de Lardizabal Pasealekua 5, 20018 Donostia/San Sebastián, Spain;
Donostia International Physics Center (DIPC), Manuel de Lardizabal Pasealekua 4, 20018 Donostia/San Sebastián, Spain
[3] Sorbonne Université, CNRS, Institut des Nanosciences de Paris, UMR7588, F-75252, Paris, France

tural searches were constrained to search for high-symmetry groups, in order to find saddle-point structures that could be stabilized by entropic or quantum effects[14]. Furthermore, many competing structures differ in enthalpy by less than 1 meV per atom in a broad range of pressures[19]. This makes the identification of the ground state very sensitive to errors difficult to control, like the choice of a particular exchange-correlation functional in density functional theory (DFT) calculations.

The presence of strong quantum fluctuations is not only crucial for the structures of hydrogen, but it also implies that large anharmonic effects shift and deform the phonon spectral functions observed with Raman and IR probes. Considering that most of the experimental signatures used to distinguish between hydrogen phases rely on the characterization of the H_2 vibron, it is mandatory to perform a fully quantum and anharmonic description of vibrational properties. Classical molecular dynamics simulations of Raman and IR spectra performed so far[20], which do consider anharmonicity but not quantum effects, strongly underestimate nuclear fluctuations and may yield to strong errors in vibron energies. In fact, vibrons, with energies above 3500 cm^{-1}, require approximately 5000 K to be thermally populated so that their quantum fluctuations are completely missed in any classical molecular dynamics simulation in the solid-state.

The difficulties in dealing with quantum nuclei lead to the existence of strange twists in the recent theoretical literature: where different exchange-correlation functionals are chosen to describe energetics[14,15,19,21,22] or vibrational features[12–14,20,23]. This is a clear sign that current theoretical methods lack the precision necessary to compare with experiments, and this is compensated with the *ad hoc* choice of the exchange-correlation functional that best fits with experimental data. However, in this way, calculations cannot be predictive and the correct assessment of the crystalline phase is built on the hope of a big error cancellation between exchange-correlation and quantum nuclear effects.

In this work we focus on hydrogen's metallization, exploring the scenario of the direct/indirect band gap closure of phase III, recently observed experimentally[2,3], as well as its Raman and IR spectra. This phase is stable above 150 GPa at low temperatures (under 200 K) and is characterized by the presence of a high infrared activity above 4000 cm^{-1}. Both the IR and the Raman vibrons are well-defined peaks that become softer and broader with increasing pressure. To include quantum and anharmonic effects on nuclei we employ the stochastic self-consistent harmonic approximation (SSCHA)[24–26]. The SSCHA performs a quantum variational minimization of the Gibbs free energy assuming that the quantum wave-functions of the nuclei can be represented as a multidimensional Gaussian, parametrized by *centroid* positions, which determine the maximum of the ionic wave-functions, and effective force constants, which determine the mean squared displacement of atoms around the centroids. By evaluating the stress tensor associated with the SSCHA energy[26], we relax the crystal structures including also lattice parameters in a fully quantum and anharmonic description. To simulate vibrational properties we exploit the dynamical extension of the SSCHA[25]. Thus, we can compute all the experimentally accessible data in a consistent way both for the structural and spectral properties.

The most supported candidate for phase III is a base-centered monoclinic structure with C2/c space group and 24 atoms in the primitive unit cell (labeled C2/c-24). The structure consists of four different layers of imperfect hexagonal rings formed by H_2 molecules (see Fig. 2, panels **d-e**). Despite its monoclinic character, the cell has a very slight distortion with respect to the hexagonal one ($\alpha = 89.9^o$, $\gamma = 119^o$, the whole structures with quantum effects are reported in the Extended Data Figure 9).We performed a constant pressure quantum relaxation at 155 GPa, 260 GPa, 355 GPa, and 460 GPa to cover the whole experimental pressure range. We report the structural modification induced by quantum fluctuations in **Figure** 2. Quantum fluctuations generate a volume expansion at fixed pressure of about 1.5% (1% at 460 GPa), but do not modify qualitatively the equation of state (panel **a**). The volume expansion is nonisotropic and acts mainly on the out-of-plane lattice parameter c, pushing away the layers as pressure is increased (panel **b**). The most important effect is on the H_2 bond length, which increases up to 6 % in comparison to the classical result (panel **c**). A similar extreme stretching was also shown in Cmca-4 hydrogen[27]. The equation of state agrees well with the experimental data from X-ray diffraction[9], while the c/a ratio is slightly underestimated (this could be related to the different temperatures of the experiment and our simulations), see Extended Data Figure 10. The classical treatment of the nuclei completely misses the dependence of the H_2 bond length with pressure in C2/c-24 hydrogen: while the bond length appears to be pressure independent in the classical calculation, it increases with pressure in the quantum calculation, showing the tendency imposed by pressure towards molecular dissociation. Considering that the molecular bond length has a huge impact both on the energy of molecular phases of hydrogen and their vibrational frequencies, no classical calculation is expected to determine accurately the phase diagram and the spectroscopic properties of high-pressure hydrogen.

We report in **Figure** 3 the simulation of the Raman and IR vibrons. Quantum fluctuations trigger the anharmonicity of the vibron by shifting the position of the peaks and introducing a finite life-time with respect to the harmonic result. The Raman vibron (panels **c,d**) acquires a very broad linewidth with increasing pressure due to anharmonic phonon-phonon scattering, in good agreement with experiments. On the other side, the IR linewidth does not increase as much as the Raman, and the broadening at 355 GPa is dominated by the LO-TO splitting. In fact, thanks to the effective charges on the IR vibron, the real part of the dielectric function remains negative above the transverse optical (TO) frequency, causing the sample to absorb in a band between the TO and longitudinal optical (LO) frequencies. This underlines the importance of considering the full dielectric tensor (summing optical and vibrational contributions) to simulate the vibrational spectrum (see Methods). The slope of the vibron energy versus pressure increases when quantum effects are considered for

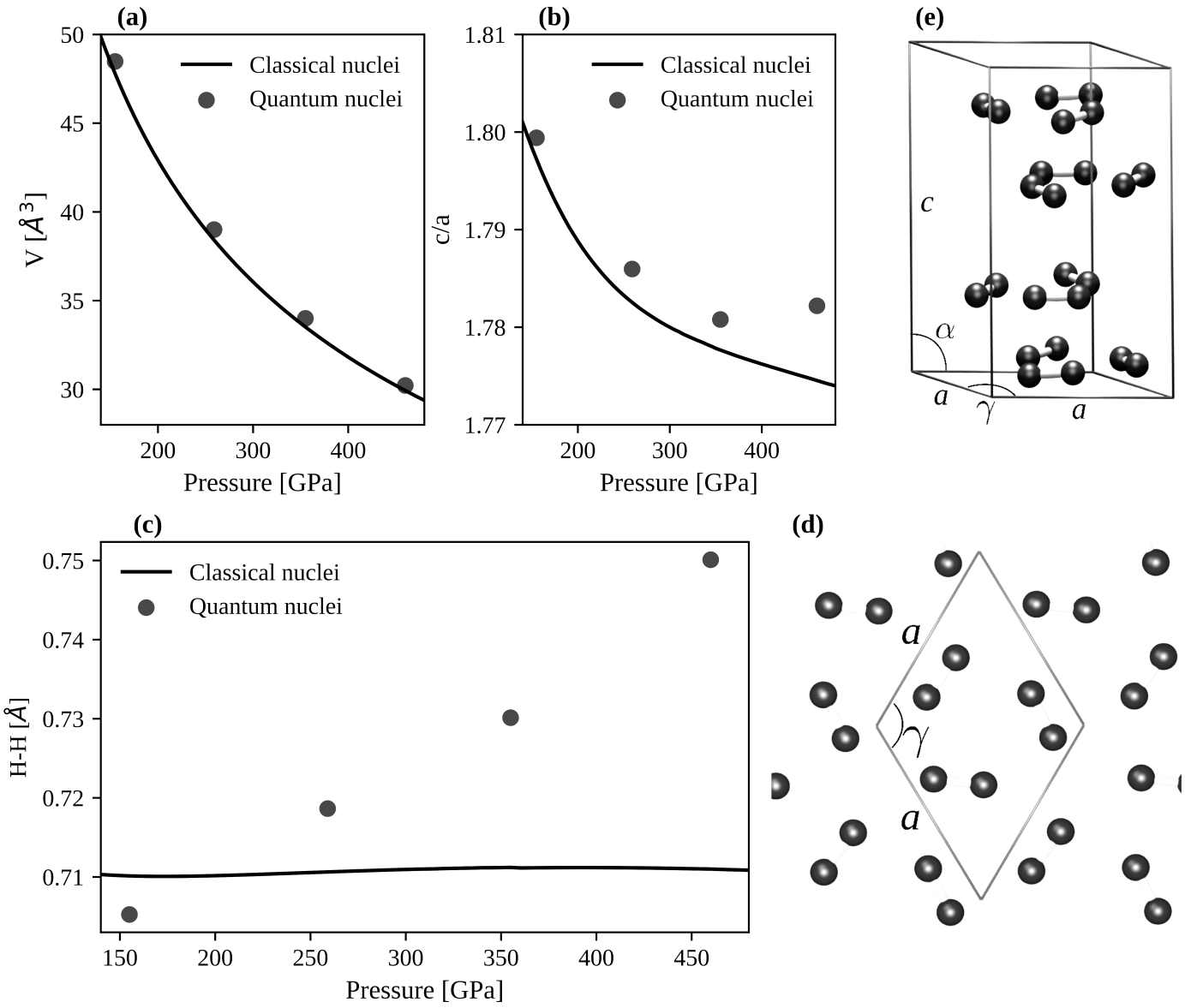

Figure 2. Crystal structure with and without quantum effects of hydrogen phase III (C2/c-24). (**a**) the equation of state. (**b**) the c/a ratio as a function of pressure. It quantifies the anisotropy of the quantum contribution to the stress tensor, more pronounced in the c direction (out-of-plane) with respect to the a vector (in-plane). (**c**) The H_2 bond length as a function of pressure. (**d**) Top view of a single layer of C2/c-24. (**e**) Primitive cell of the C2/c-24 phase.

both Raman and IR simulations (panels **e,f**). This is a consequence of the tendency towards dissociation of the H_2 molecules, whose increasing bond-length with pressure is missed by the static theory (**Figure** 2, panel **c**). At 300 GPa we predict a slope for the IR vibron of $-1.96\,\mathrm{cm^{-1}\,GPa^{-1}}$ (harmonic $-0.71\,\mathrm{cm^{-1}\,GPa^{-1}}$) increasing the match with the experimental one of $-2.46\,\mathrm{cm^{-1}\,GPa^{-1}}$. Also the agreement of the Raman vibron slope is improved: we predict a value of $-3.49\,\mathrm{cm^{-1}\,GPa^{-1}}$ (harmonic $-1.32\,\mathrm{cm^{-1}\,GPa^{-1}}$) versus the experimental one of $-3.02\,\mathrm{cm^{-1}\,GPa^{-1}}$. All the spectra that include quantum fluctuations show a quantitative improvement with respect to the harmonic simulation. The vibron gets much closer to the experimental value, and the line-shape is very well reproduced. Even if we are slightly underestimating the vibrational energy, our results support C2/c-24 as phase III of hydrogen. We believe this slight underestimation is a residual consequence of the choice of the exchange and correlation functional, even if the BLYP functional we use is recognized among the most accurate for predicting energies of high-pressure hydrogen[21] and it is commonly chosen for the calculation of the hydrogen phase-diagram[14,19]. The huge peak shift and the change in the slope of the vibron frequency caused by the zero-point motion question the validity of previous calculations that do not include both anharmonicity and quantum nuclear fluctuations[12–14,20,28].

Even if our quantum anharmonic calculations support C2/c-24 as phase III of hydrogen, it is not obvious if it

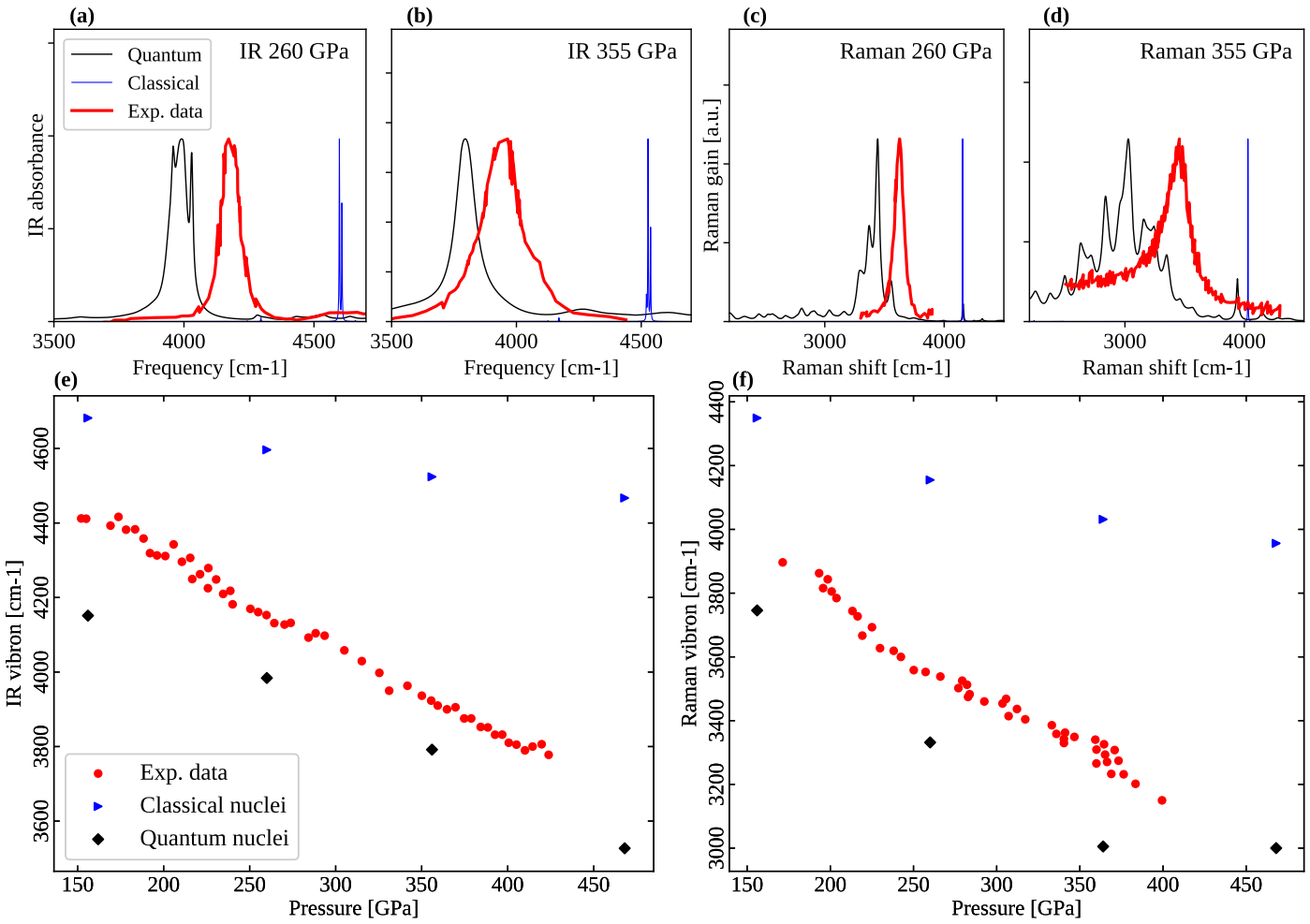

Figure 3. Vibrational spectra at 0 K. Panels **(a-b)**: Simulation of the IR absorbance within the harmonic approximation (classical nuclei), full quantum anharmonic theory and experimental data (Ref.[3] at 251 GPa and 351 GPa at 80 K). A small smearing has been added to the harmonic spectrum for presentation purposes. Panel **(c-d)**: Simulation of the Raman spectra, experimental data from Ref.[10] (248 GPa at 140 K) and Ref.[2] (360 GPa and 100 K). Panel **(e)**: Position of the IR vibron peak vs pressure. Exp. data from[3] (80 K). Panel **(e)**: Raman vibron peak vs pressure. Exp. data from[2].

can explain the apparent contradictions between different experiments on the metallization. To clarify this issue, we compute the optical properties of C2c-24 hydrogen including the electron-phonon interaction beyond perturbation theory. We use the SSCHA quantum wave-function to extract a supercell phonon-distorted configuration to compute the dielectric properties (see Methods). We use supercells with 432 atoms, that are much larger than those used in prior studies (96 atoms)[15,29]. The impact of the electron-phonon interaction on electronic and optical properties converges slowly with the cell size. The use of a small cell leads to overestimating the DOS at the Fermi energy, the plasma frequency, and underestimating the metallization pressure (see Extended Data Figure 1 and 2). To correct the systematic underestimation of the DFT band gap in the optical properties, we went beyond DFT employing the TB09 meta-GGA[30], a functional esplicitly developed to calculate the electronic band structure, which is known to reach almost the GW accuracy on a broad data-set of materials[31]. To estimate the error on the choice of the functional for the band gap, we repeated the same calculations within DFT correcting the gap with a constant scissor value as described in ref.[32], showing a discrepancy of about 0.3 eV (see Extended Data Figure 6).

The closure of the gap in the density of states (DOS) coincides with the onset of conductivity. Here this occurs at 380 GPa (see **Figure** 4, panels **a,d**) at 0 K, in good agreement with the conductivity measurements in Ref.[2] (360 GPa at 200 K). However, after the fundamental gap closes, the Drude peak is small (due to the small value of the DOS), as we show in panel **(e)**. Thus, the sample remains transparent within an IR window that extends up to the direct gap energy associated with interband optical transitions (panel **b**). The low DOS around the Fermi level of phase III (panel **a** of **Figure** 4) indicates that this phase will not be a high-temperature superconductor. The closure of the predicted optical gap matches nicely with the measurements of Ref.[3] (panel **d**), and it is in agree-

ment with another recent theoretical work which employed a different methodology[33]. Finally, even above the metallic transition and the optical gap closure, reflectivity in the optical range is very flat and small because of interband transitions (panel **c**). This gives a dark appearance to the sample, as observed in experiments.

From the remarkable agreement with experiments, our calculations support the C2/c-24 structure as the phase III also from optical properties, at odds with previous results[15]. Interestingly, we find quantum fluctuations to have a stronger impact on the optical gap, downshifted by more than 3 eV, while the fundamental indirect gap is downshifted by about 2 eV.

In **Figure** 4 (**d**) we predict the metallization of deuterium. The indirect gap increases by 1 eV and the optical by about 1.2 eV with respect to protium at 0 K. However, since deuterium has lower phonon energy modes, its band structure is expected to be more affected by temperature than protium. This isotope effect on the electronic properties is the largest we are aware of in a solid crystal. If no phase-transitions occurs, deuterium should become a black metal at 450 GPa, 70 GPa higher than protium.

Our calculations show that there is no contradiction between the existence of a conducting metallic state, an IR transparent window, and a black appearance of the sample. As our results predict a low reflectivity at 460 GPa, we rule out the hypothesis of C2/c-24 becoming shiny at very high pressure, and the claimed metallization observed at 490 GPa must be related to a first-order phase-transition[1], probably to an atomic metallic phase[34].

Acknowledgements
L.M. acknowledges the CINECA award under the ISCRA initiative, for the availability of high performance computing resources and support. This work was performed using HPC resources from Idris and The Grand Challenge Jean Zay. I.E. has received funding from the European Research Council (ERC) under the European Unions Horizon 2020 research and innovation program (grant agreement No. 802533).

Author contributions
The project was conceived by all authors. L.M. made the analytical and numerical calculations and prepared the figures with inputs from all the authors. All authors contributed to the redaction of the manuscript.

Competing interests
The authors declare no competing interests.

Data availability statement
Source data are available for this paper. All other data that support the plots within this paper and other findings of this study are available from the corresponding author upon reasonable request.

Code availability statement
The source code used to implement the SSCHA is currently under release with GPLv3 license, and will be made available soon. The source code to compute the dielectric function in Eq. (6) is a custom version of Quantum ESPRESSO and it is available in GitLab: https://gitlab.com/mesonepigreco/q-e

Additional information
Correspondence and request of materials should be addressed to F.M.

Methods

To include quantum fluctuations and anharmonicity at a non-perturbative level, we use the stochastic self-consistent harmonic approximation (SSCHA)[24–26]. The SSCHA is a variational method: it looks for the density matrix that minimizes the Gibbs free energy:

$$G(P,T) = \min_{\tilde{\rho}} \mathrm{Tr}\left[\tilde{\rho}H + k_b T \tilde{\rho}\ln\tilde{\rho} + P\Omega(\tilde{\rho})\right], \qquad (1)$$

where $\Omega(\rho)$ is the crystal volume, H is the ionic Hamiltonian in the Born-Oppenheimer approximation,

$$H = T + V, \qquad (2)$$

with T the ionic kinetic energy and V the energy landscape. The trial density matrix $\tilde{\rho}$ is chosen among all possible Gaussians. In this way, the only variational parameters are the average centroid positions and the fluctuations around the average.

The energy landscape V is calculated within density functional theory (DFT) using the generalized gradient approximation (GGA) BLYP[35], as implemented in Quantum ESPRESSO[36,37]. The static and dynamical SSCHA calculations were performed in a $2\times2\times1$ supercell of the primitive unit cell, which consists of 96 atoms. Each supercell configuration was computed with a uniform grid of $4\times4\times4$ for the Brillouin zone integrals, with a wave-function cutoff of 60 Ry (240 Ry for the electronic density). The convergence of results was checked with a $6\times6\times6$ grid and a wave-function cutoff of 80 Ry (320 Ry for the density). We generated a norm-conserving pseudo-potential with no pseudized electrons using the settings from the Pseudo Dojo[38] library and the ONCVPSP software[39]. In all calculations, Marzari-Vanderbilt smearing of 0.03 Ry was used to account for the enhanced gap closure in the 96 atom cell when the phonon-distorted configuration is considered (see SI).

The indirect band gap is computed from the electron DOS, as shown in **Figure** 4 (panel **a**). The DOS is obtained simulating a configuration with 432 atoms ($3\times3\times2$ supercell) with ions randomly distributed according to the SSCHA nuclear wave-function. The electronic states are obtained through a DFT calculation with TB09 functional as implemented in Quantum ESPRESSO[40], with a Brillouin zone sampling of $8\times8\times6$. Interestingly, we find TB09 to reproduce the fundamental band gap for the ideal crystal (open squares in **Figure** 4, panel **d**) in very good agreement with G_0W_0 calculations of Ref.[22] and Quantum Monte Carlo of Ref.[32], with a computational cost re-

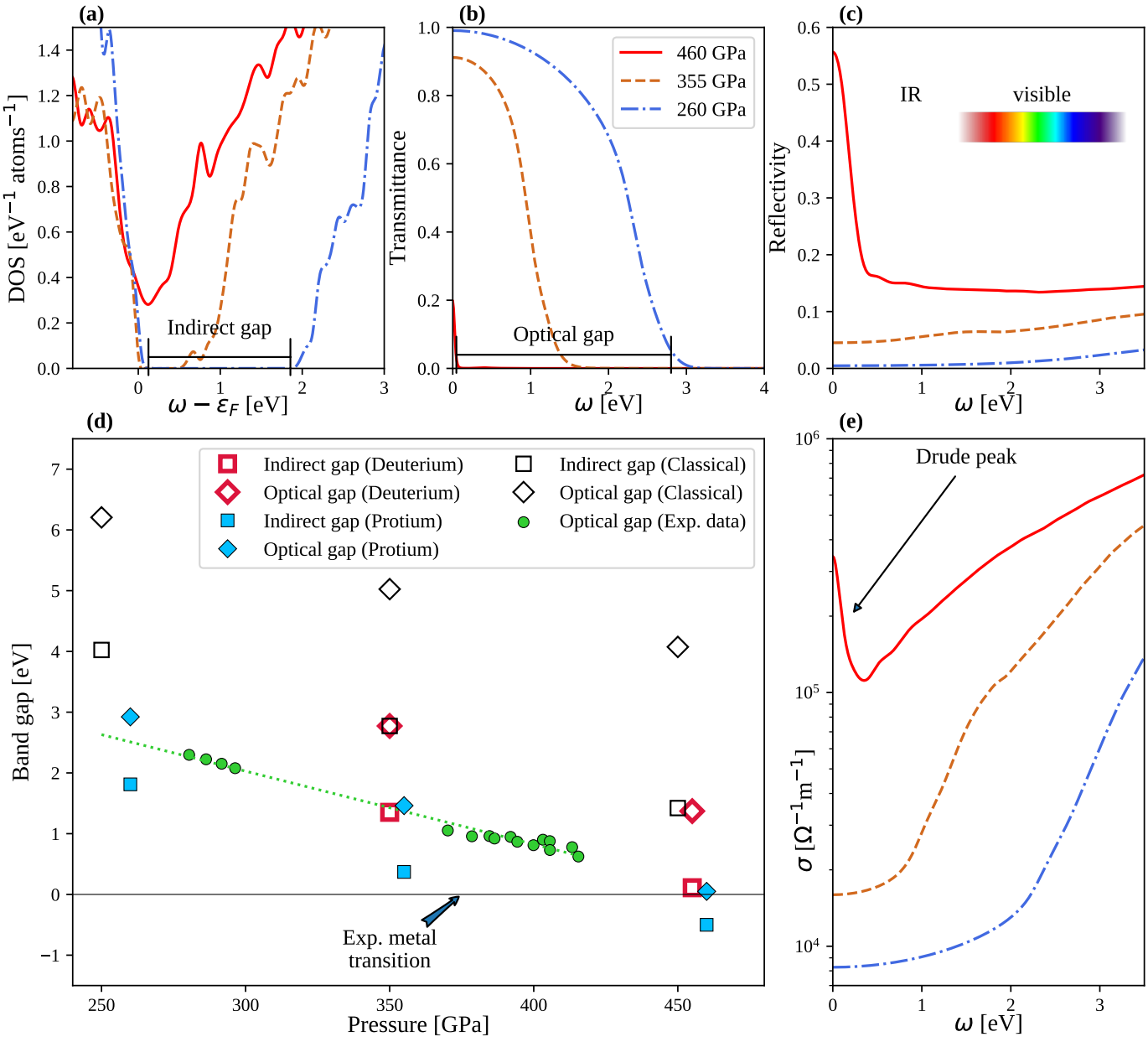

Figure 4. Optical properties of phase III of hydrogen, including quantum nuclear fluctuations, sampled in a supercell with 432 atoms. **(a)** Electron DOS at three pressures (protium). The indirect gap is measured as the region where the DOS per atom drops below 0.001 eV^{-1}. **(b)** Transmittance over a sample of 1.5 µm (protium). The transmittance is used to compute the direct (optical) gap as shown by the bars for the case of 260 GPa. **(c)** Reflectivity of hydrogen at different pressures (protium). Even if the phase is a metal above 375 GPa, the reflectivity in the IR remains very low (under 20% at 460 GPa) in the whole visible range (marked with a rainbow). So we predict the phase to be transparent at 250 GPa, black at 355 GPa and remaining black even at higher pressures, where also the optical gap is closed. **(d)** The indirect and direct gap for protium, deuterium and the classical nuclei (infinite mass), compared with the experimental results[3]. The metallic transition due to indirect gap closure occurs experimentally (protium) at 360 GPa at 200 K[2]. We refer to "classical" the gaps computed in the static equilibrium configuration, while for protium and deuterium (hydrogen-1 and 2) the optical properties computed in a snapshot sampled from the quantum nuclei wave-function (see Methods). **(e)** Optical conductivity (protium). For clarity, in panels (**b,c,e**) we report the data considering only the electronic contribution to the susceptibility (see Methods).

duced of many orders of magnitude. Our optical calculations differ from Ref.[33]: we employed a bigger simulation cell, accounted for non vertical electronic transition due to electron-phonon coupling, and neglected dynamical effects. The direct gap is computed from the simulated transmittance over a sample of 1.5 µm, as illustrated in **Figure** 4 (panel **b**). The dielectric tensor and the optical conductivity,

$$\varepsilon^{(tot)}(\omega) = 1 + 4\pi\chi^{(tot)}(\omega) \tag{3}$$

and

$$\boldsymbol{\sigma}^{(tot)}(z) = -iz\boldsymbol{\chi}^{(tot)}(z), \tag{4}$$

are computed from the total susceptibility. This is divided into an electronic and a ionic contribution:

$$\boldsymbol{\chi}^{(tot)} = \boldsymbol{\chi} + \boldsymbol{\chi}^{(ion)}. \tag{5}$$

All the quantities with $^{(tot)}$ are computed accounting for both the ionic and electronic contribution, otherwise only the electronic contribution is included. The electronic susceptibility is computed within the independent particle approximation framework on the same phonon-displaced configuration as the DOS. We checked that the results did not change if the operation is repeated in 5 different configurations.

$$\chi_{\alpha\beta}(z) = -\frac{2e^2}{m^2 N_k \Omega} \sum_{kmn} \frac{f(\xi_{km}) - f(\xi_{km})}{\xi_{km} - \xi_{kn}} \frac{\langle km|p_\alpha|kn\rangle \langle kn|p_\beta|km\rangle}{(\varepsilon_{km} - \varepsilon_{kn})^2 - z^2}, \tag{6}$$

$$\xi_{km} = \varepsilon_{km} - \varepsilon_f \qquad z = \omega + i\eta, \tag{7}$$

where N_k is the number of k points used in the sum, Ω the simulation cell volume, f the Fermi occupation function, ε_{kn} and ε_f, respectively, the energy of the state $|kn\rangle$ and the Fermi energy, η the smearing, and $\langle km|p_\alpha|kn\rangle$ is the momentum matrix element along the Cartesian direction α for the optical transition between the m and n states at the k point in the reciprocal space. Eq. (6) includes both interband and intraband terms, enabling to correctly simulate the disordered phonon displaced configurations in the supercell even when interband and intraband transitions are not well defined. We implemented Eq. (6) into the epsilon.x code of Quantum Espresso. We used a smearing η of 0.1 eV (this is the reason for the non zero conductivity of the insulating phase of **Figure** 4). To account for all possible orientations of the crystal we take

$$\epsilon(\omega) = \frac{1}{3} \sum_{\alpha=x,y,z} \epsilon_{\alpha\alpha}(\omega). \tag{8}$$

The refractive index of the material is

$$n(\omega) = \sqrt{\varepsilon(\omega)}. \tag{9}$$

The reflectivity of **Figure** 4 (panel **c**) is computed as

$$R = \left| \frac{n(\omega) - n_d}{n(\omega) + n_d} \right|^2, \tag{10}$$

where n_d is the diamond anvil cell refractive index, that is assumed constant in the simulated interval to 2.33. The transmittance across a sample of thickness $d = 1.5\,\mu$m is simulated as

$$T = (1-R)^2 \exp\left(-2\omega \Im n \frac{d}{c}\right), \tag{11}$$

(we neglected multiple reflections inside the sample). The optical band gap is considered as the first value for which the transmittance drops below 2% (excluding the absorption due to the vibrational modes). In **Figure** 4, the ionic contribution to conductivity, transmittance, and reflectivity was neglected. However, it is important to simulate the vibrational spectrum. The ionic susceptibility is the dipole-dipole correlation function:

$$\chi^{(ion)}_{\alpha\beta}(\omega) = \int_{-\infty}^{\infty} e^{-i\omega t} \langle M_\alpha(t) M_\beta(0)\rangle \, dt. \tag{12}$$

The average $\langle\cdot\rangle$ must be performed on the quantum nuclear ground state. The dipole induced by a ionic displacement is approximated as linear:

$$M_\alpha(t) = |e| \sum_{b=1}^{3N} Z_{\alpha b}[R_b(t) - R_b^{(0)}], \tag{13}$$

where $Z_{\alpha b}$ is the Born effective charge, $R_b(t)$ is the position operator of the b atom and $R_b^{(0)}$ is the average position of the b atom (b runs over both atomic and Cartesian indices). In **Figure** 3 (panels **a,b**), we report the IR vibron signal computed as the difference of the transmittance with and without the ionic contribution. This quantity correctly accounts for electrostatic effects neglected by just considering the imaginary part of the susceptibility. In particular, the sample absorbs where the refractive index (Eq. 9) has an imaginary part. When the ionic contribution is negligible with respect to the electronic one, the complex refractive index may be approximated as:

$$n^{(tot)}(\omega) \approx n + \frac{2\pi}{n}\chi^{(ion)} \qquad 4\pi\chi^{(ion)} \ll 1 + 4\pi\chi \tag{14}$$

For a transparent material (i.e. the imaginary part of n is zero: $\Im n = 0$), the absorption is directly related to the imaginary part of the ionic susceptibility:

$$\Im n^{(tot)}(\omega) \approx \frac{2\pi}{n} \Im\chi^{(ion)}(\omega) \tag{15}$$

However, in the presence of strong effective charges, the ionic susceptibility can be greater than the electronic one. In this case also the real part of $\chi^{(ion)}$ gives a contribution to the absorption. In particular, ε becomes negative between the LO and the TO frequencies. This induces absorption (see Eq. (9)) in a finite region even in the presence of a phonon with an infinite lifetime. This is a dominant contribution to the IR vibron at 355 GPa (see Extended Data Figure 3).

The Raman spectrum is assumed proportional to the polarizability correlation function:

$$I_{Raman}(\omega) \propto \Im \int_{-\infty}^{\infty} dt e^{-i\omega t} \langle \boldsymbol{\alpha}(t)\boldsymbol{\alpha}(0)\rangle, \tag{16}$$

$$\alpha_{ab}(t) = \sum_{c=1}^{3N} A_{\alpha\beta c}[R_c(t) - R_c^{(0)}], \tag{17}$$

here, A is the Raman tensor. The position operator in both Eq. (13) and (17) can be written using phonon creation-annihilation operators. The resulting phonon correlation functions of Eq. (12) and Eq. (16) are computed using the SSCHA dynamical Green function[25], accounting for phonon-phonon interactions non perturbatively. For the IR we get:

$$\chi_{\alpha\beta}^{(ion)}(\omega) = e^2 \sum_{ab} \frac{Z_{\alpha a} Z_{\beta b}}{\sqrt{m_a m_b}} G_{ab}(\omega), \tag{18}$$

$$\frac{G_{ab}(t)}{\sqrt{m_a m_b}} = \langle [R_a(t) - R_a^{(0)}][R_b(0) - R_b^{(0)}] \rangle \,, \tag{19}$$

$$G_{ab}^{-1}(\omega) = \omega^2 - D_{ab} - \Pi_{ab}(\omega), \tag{20}$$

$\boldsymbol{D}$ is the SCHA dynamical matrix, $\boldsymbol{\Pi}$ is the phonon self-energy (Ref.[41] equation A12), m_a is the atomic mass of the a-th atom.Eq. (20) has been computed using a Lanczos algorithm that will be discussed elsewhere in detail. Noten Eq. (18) we trace the Green function $G_{ab}(\omega)$ contracted with the effective charges and we keep both the real and imaginary part to study the absorption, after summing the electronic contribution to it (Eq. 6). For the Raman calculation, we instead take the imaginary part of the response function:

$$I_{Raman}(\omega) \propto -\sum_{\alpha=1}^{3} \sum_{ab} \frac{A_{\alpha\alpha a} A_{\alpha\alpha b}}{\sqrt{m_a m_b}} \Im G_{ab}(\omega). \tag{21}$$

Here, we consider only the Raman contribution arising by incoming and outcoming radiation with the same polarization vector. Also in this case, the Green function is contracted with the Raman tensor.

In the self-energy expression $\boldsymbol{\Pi}(\omega)$, we compared the results with and without the 4 phonon scattering vertex (the $\overset{(4)}{\boldsymbol{\Phi}}$ of Ref.[41] equation A12), obtaining no significative difference. Thus, all the simulations have been performed setting $\overset{(4)}{\boldsymbol{\Phi}} = 0$ ($\boldsymbol{\Pi}(\omega)$ reduces to equation A14 of Ref.[41]). The effective charges and the Raman tensor of Eq. (13) and (17) are computed with Quantum ESPRESSO phonon packages in the SSCHA average centroid position. The Raman tensor was computed within the LDA approximation[42]. For the 460 GPa calculation, we computed the Raman tensor and effective charges forcing the system to be an insulator, thus our results are indicative. A more sophisticated time-dependent approach should be used for metals to correctly describe them[43].

[1] R. P. Dias and I. F. Silvera, "Observation of the wigner-huntington transition to metallic hydrogen," *Science*, vol. 355, pp. 715–718, 2017.

[2] M. I. Eremets, A. P. Drozdov, P. P. Kong, and H. Wang, "Semimetallic molecular hydrogen at pressure above 350 GPa," *Nature Physics*, vol. 15, pp. 1246–1249, 2019.

[3] P. Loubeyre, F. Occelli, and P. Dumas, "Synchrotron infrared spectroscopic evidence of the probable transition to metal hydrogen," *Nature*, vol. 577, pp. 631–635, 2020.

[4] H.-k. Mao and R. J. Hemley, "Ultrahigh-pressure transitions in solid hydrogen," *Reviews of modern physics*, vol. 66, no. 2, p. 671, 1994.

[5] R. T. Howie, C. L. Guillaume, T. Scheler, A. F. Goncharov, and E. Gregoryanz, "Mixed molecular and atomic phase of dense hydrogen," *Physical Review Letters*, vol. 108, p. 125501, 2012.

[6] P. Dalladay-Simpson, R. T. Howie, and E. Gregoryanz, "Evidence for a new phase of dense hydrogen above 325 gigapascals," *Nature*, vol. 529, pp. 63–67, 2016.

[7] E. Wigner and H. B. Huntington, "On the possibility of a metallic modification of hydrogen," *The Journal of Chemical Physics*, vol. 3, pp. 764–770, 1935.

[8] N. W. Ashcroft, "Metallic hydrogen: A high-temperature superconductor?," *Phys. Rev. Lett.*, vol. 21, pp. 1748–1749, 1968.

[9] C. Ji, B. Li, W. Liu, J. S. Smith, A. Majumdar, W. Luo, R. Ahuja, J. Shu, J. Wang, S. Sinogeikin, Y. Meng, V. B. Prakapenka, E. Greenberg, R. Xu, X. Huang, W. Yang, G. Shen, W. L. Mao, and H.-K. Mao, "Ultrahigh-pressure isostructural electronic transitions in hydrogen," *Nature*, vol. 573, pp. 558–562, 2019.

[10] A. F. Goncharov and V. V. Struzhkin, "Comment on "observation of the wigner-huntington transition to metallic hydrogen"," *Science*, vol. 357, no. 6353, 2017.

[11] J. Kohanoff, S. Scandolo, G. L. Chiarotti, and E. Tosatti, "Solid molecular hydrogen: The broken symmetry phase," *Physical Review Letters*, vol. 78, pp. 2783–2786, 1997.

[12] C. J. Pickard and R. J. Needs, "Structure of phase III of solid hydrogen," *Nature Physics*, vol. 3, pp. 473–476, 2007.

[13] C. J. Pickard, M. Martinez-Canales, and R. J. Needs, "Density functional theory study of phase iv of solid hydrogen," *Phys. Rev. B*, vol. 85, p. 214114, 2012.

[14] B. Monserrat, N. D. Drummond, P. Dalladay-Simpson, R. T. Howie, P. L. Ríos, E. Gregoryanz, C. J. Pickard, and R. J. Needs, "Structure and metallicity of phase v of hydrogen," *Physical Review Letters*, vol. 120, 2018.

[15] S. Azadi, R. Singh, and T. D. Kühne, "Nuclear quantum effects induce metallization of dense solid molecular hydrogen," *Journal of Computational Chemistry*, vol. 39, pp. 262–268, 2017.

[16] I. Errea, M. Calandra, C. J. Pickard, J. R. Nelson, R. J. Needs, Y. Li, H. Liu, Y. Zhang, Y. Ma, and F. Mauri, "Quantum hydrogen-bond symmetrization in the superconducting hydrogen sulfide system," *Nature*, vol. 532, pp. 81–84, 2016.

[17] I. Errea, F. Belli, L. Monacelli, A. Sanna, T. Koretsune, T. Tadano, R. Bianco, M. Calandra, R. Arita, F. Mauri, and J. A. Flores-Livas, "Quantum crystal structure in the 250-kelvin superconducting lanthanum hydride," *Nature*, vol. 578, pp. 66–69, 2020.

[18] D. M. Straus and N. W. Ashcroft, "Self-consistent structure of metallic hydrogen," *Physical Review Letters*, vol. 38, pp. 415–418, 1977.

[19] N. D. Drummond, B. Monserrat, J. H. Lloyd-Williams, P. L. Ríos, C. J. Pickard, and R. J. Needs, "Quantum monte carlo study of the phase diagram of solid molecular hydrogen at extreme pressures," *Nature Communications*, vol. 6, p. 7794, 2015.

[20] I. B. Magdău and G. J. Ackland, "Identification of high-pressure phases III and IV in hydrogen: Simulating raman spectra using molecular dynamics," *Physical Review B*, vol. 87, p. 174110, 2013.

[21] R. C. Clay, J. Mcminis, J. M. McMahon, C. Pierleoni, D. M. Ceperley, and M. A. Morales, "Benchmarking exchange-correlation functionals for hydrogen at high pressures using quantum monte carlo," *Physical Review B*, vol. 89, p. 184106, 2014.

[22] J. McMinis, R. C. Clay, D. Lee, and M. A. Morales, "Molecular to atomic phase transition in hydrogen under high pressure," *Physical Review Letters*, vol. 114, p. 105305, 2015.

[23] R. Singh, S. Azadi, and T. D. Kühne, "Anharmonicity and finite-temperature effects on the structure, stability, and vibrational spectrum of phase III of solid molecular hydrogen," *Physical Review B*, vol. 90, p. 014110, 2014.

[24] I. Errea, M. Calandra, and F. Mauri, "Anharmonic free energies and phonon dispersions from the stochastic self-consistent harmonic approximation: Application to platinum and palladium hydrides," *Physical Review B*, vol. 89, p. 064302, 2014.

[25] R. Bianco, I. Errea, L. Paulatto, M. Calandra, and F. Mauri, "Second-order structural phase transitions, free energy curvature, and temperature-dependent anharmonic phonons in the self-consistent harmonic approximation: Theory and stochastic implementation," *Physical Review B*, vol. 96, p. 014111, 2017.

[26] L. Monacelli, I. Errea, M. Calandra, and F. Mauri, "Pressure and stress tensor of complex anharmonic crystals within the stochastic self-consistent harmonic approximation," *Phys. Rev. B*, vol. 98, p. 024106, 2018.

[27] M. Borinaga, P. Riego, A. Leonardo, M. Calandra, F. Mauri, A. Bergara, and I. Errea, "Anharmonic enhancement of superconductivity in metallic molecularCmca - 4 hydrogen at high pressure: a first-principles study," *Journal of Physics: Condensed Matter*, vol. 28, p. 494001, 2016.

[28] C. Zhang, C. Zhang, M. Chen, W. Kang, Z. Gu, J. Zhao, C. Liu, C. Sun, and P. Zhang, "Finite-temperature infrared and raman spectra of high-pressure hydrogen from first-principles molecular dynamics," *Physical Review B*, vol. 98, p. 144301, 2018.

[29] G. Rillo, M. A. Morales, D. M. Ceperley, and C. Pierleoni, "Coupled electron-ion monte carlo simulation of hydrogen molecular crystals," *The Journal of Chemical Physics*, vol. 148, p. 102314, 2018.

[30] F. Tran and P. Blaha, "Accurate band gaps of semiconductors and insulators with a semilocal exchange-correlation potential," *Physical Review Letters*, vol. 102, p. 226401, 2009.

[31] P. Borlido, T. Aull, A. W. Huran, F. Tran, M. A. L. Marques, and S. Botti, "Large-scale benchmark of exchange–correlation functionals for the determination of electronic band gaps of solids," *Journal of Chemical Theory and Computation*, vol. 15, pp. 5069–5079, 2019.

[32] S. Azadi, N. D. Drummond, and W. M. C. Foulkes, "Nature of the metallization transition in solid hydrogen," *Physical Review B*, vol. 95, p. 035142, 2017.

[33] V. Gorelov, M. Holzmann, D. M. Ceperley, and C. Pierleoni, "Energy gap closure of crystalline molecular hydrogen with pressure," *Physical Review Letters*, vol. 124, p. 116401, 2020.

[34] M. Borinaga, J. Ibañez-Azpiroz, A. Bergara, and I. Errea, "Strong electron-phonon and band structure effects in the optical properties of high pressure metallic hydrogen," *Physical Review Letters*, vol. 120, p. 057402, 2018.

[35] B. Miehlich, A. Savin, H. Stoll, and H. Preuss, "Results obtained with the correlation energy density functionals of becke and lee, yang and parr," *Chemical Physics Letters*, vol. 157, no. 3, pp. 200–206, 1989.

[36] P. Giannozzi, S. Baroni, N. Bonini, M. Calandra, R. Car, C. Cavazzoni, D. Ceresoli, G. L. Chiarotti, M. Cococcioni, I. Dabo, A. D. Corso, S. de Gironcoli, S. Fabris, G. Fratesi, R. Gebauer, U. Gerstmann, C. Gougoussis, A. Kokalj, M. Lazzeri, L. Martin-Samos, N. Marzari, F. Mauri, R. Mazzarello, S. Paolini, A. Pasquarello, L. Paulatto, C. Sbraccia, S. Scandolo, G. Sclauzero, A. P. Seitsonen, A. Smogunov, P. Umari, and R. M. Wentzcovitch, "QUANTUM ESPRESSO: a modular and open-source software project for quantum simulations of materials," *Journal of Physics: Condensed Matter*, vol. 21, p. 395502, 2009.

[37] P. Giannozzi, O. Andreussi, T. Brumme, O. Bunau, M. B. Nardelli, M. Calandra, R. Car, C. Cavazzoni, D. Ceresoli, M. Cococcioni, N. Colonna, I. Carnimeo, A. D. Corso, S. de Gironcoli, P. Delugas, R. A. DiStasio, A. Ferretti, A. Floris, G. Fratesi, G. Fugallo, R. Gebauer, U. Gerstmann, F. Giustino, T. Gorni, J. Jia, M. Kawamura, H.-Y. Ko, A. Kokalj, E. Küçükbenli, M. Lazzeri, M. Marsili, N. Marzari, F. Mauri, N. L. Nguyen, H.-V. Nguyen, A. O. de-la Roza, L. Paulatto, S. Poncé, D. Rocca, R. Sabatini, B. Santra, M. Schlipf, A. P. Seitsonen, A. Smogunov, I. Timrov, T. Thonhauser, P. Umari, N. Vast, X. Wu, and S. Baroni, "Advanced capabilities for materials modelling with quantum ESPRESSO," *Journal of Physics: Condensed Matter*, vol. 29, p. 465901, 2017.

[38] M. van Setten, M. Giantomassi, E. Bousquet, M. Verstraete, D. Hamann, X. Gonze, and G.-M. Rignanese, "The PseudoDojo: Training and grading a 85 element optimized norm-conserving pseudopotential table," *Computer Physics Communications*, vol. 226, pp. 39–54, 2018.

[39] D. R. Hamann, "Optimized norm-conserving vanderbilt pseudopotentials," *Physical Review B*, vol. 88, 2013.

[40] É. Germaneau, G. Su, and Q.-R. Zheng, "Implementation of the modified becke–johnson meta-GGA functional in quantum espresso," *Computer Physics Communications*, vol. 184, pp. 1697–1700, 2013.

[41] R. Bianco, I. Errea, M. Calandra, and F. Mauri, "High-pressure phase diagram of hydrogen and deuterium sulfides from first principles: Structural and vibrational properties including quantum and anharmonic effects," *Physical Review B*, vol. 97, p. 214101, 2018.

[42] M. Lazzeri and F. Mauri, "First-principles calculation of vibrational raman spectra in large systems: Signature of small rings in CrystallineSiO2," *Physical Review Letters*, vol. 90, p. 036401, 2003.

[43] O. Bistoni, P. Barone, E. Cappelluti, L. Benfatto, and F. Mauri, "Giant effective charges and piezoelectricity in gapped graphene," *2D Materials*, vol. 6, p. 045015, 2019.

Black metal hydrogen above 360 GPa driven by proton quantum fluctuations

Lorenzo Monacelli

Department of Physics, University of "Sapienza", Rome, Italy

Ion Errea

Fisika Aplikatua 1 Saila, Gipuzkoako Ingeniaritza Eskola,
University of the Basque Country (UPV/EHU),
Europa Plaza 1, 20018, Donostia/San Sebastián, Spain
Centro de Física de Materiales (CSIC-UPV/EHU),
Manuel de Lardizabal Pasealekua 5,
20018 Donostia/San Sebastián, Spain and
Donostia International Physics Center (DIPC),
Manuel de Lardizabal Pasealekua 4,
20018 Donostia/San Sebastián, Spain

Matteo Calandra

Sorbonne Université, CNRS, Institut des Nanosciences
de Paris, UMR7588, F-75252, Paris, France

Francesco Mauri

Department of Physics, University of "La Sapienza", Rome, Italy

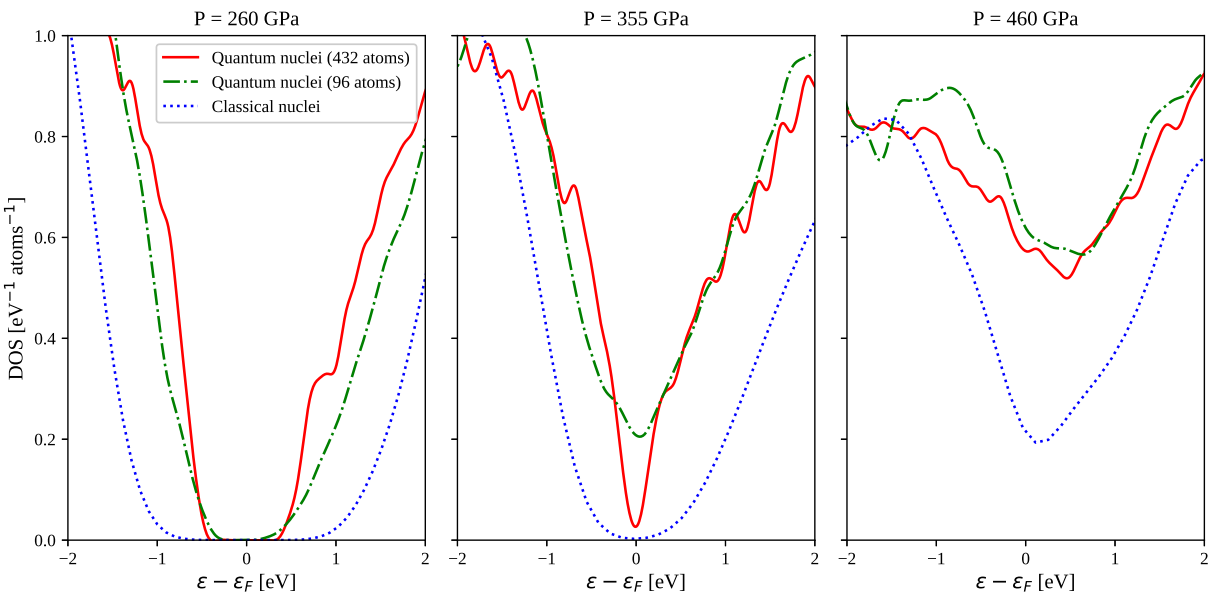

Extended Data Figure 1. Comparison of the electronic density of states with different simulation boxes (compared with the classical nuclei). The use of a small simulation cell (like the one of 96 atoms), leads to a strong underestimation of the metallic transition, as it introduces metallic states inside the gap. These simulations have been performed using the BLYP functional, thus the overall gap differs from the one of TB09 reported in the main text.

[1] P. Borlido, T. Aull, A. W. Huran, F. Tran, M. A. L. Marques, and S. Botti, Journal of Chemical Theory and Computation **15**, 5069 (2019).

[2] S. Azadi, N. D. Drummond, and W. M. C. Foulkes, Physical Review B **95**, 035142 (2017).

[3] C. Ji, B. Li, W. Liu, J. S. Smith, A. Majumdar, W. Luo, R. Ahuja, J. Shu, J. Wang, S. Sinogeikin, Y. Meng, V. B. Prakapenka, E. Greenberg, R. Xu, X. Huang, W. Yang, G. Shen, W. L. Mao, and H.-K. Mao, Nature **573**, 558 (2019).

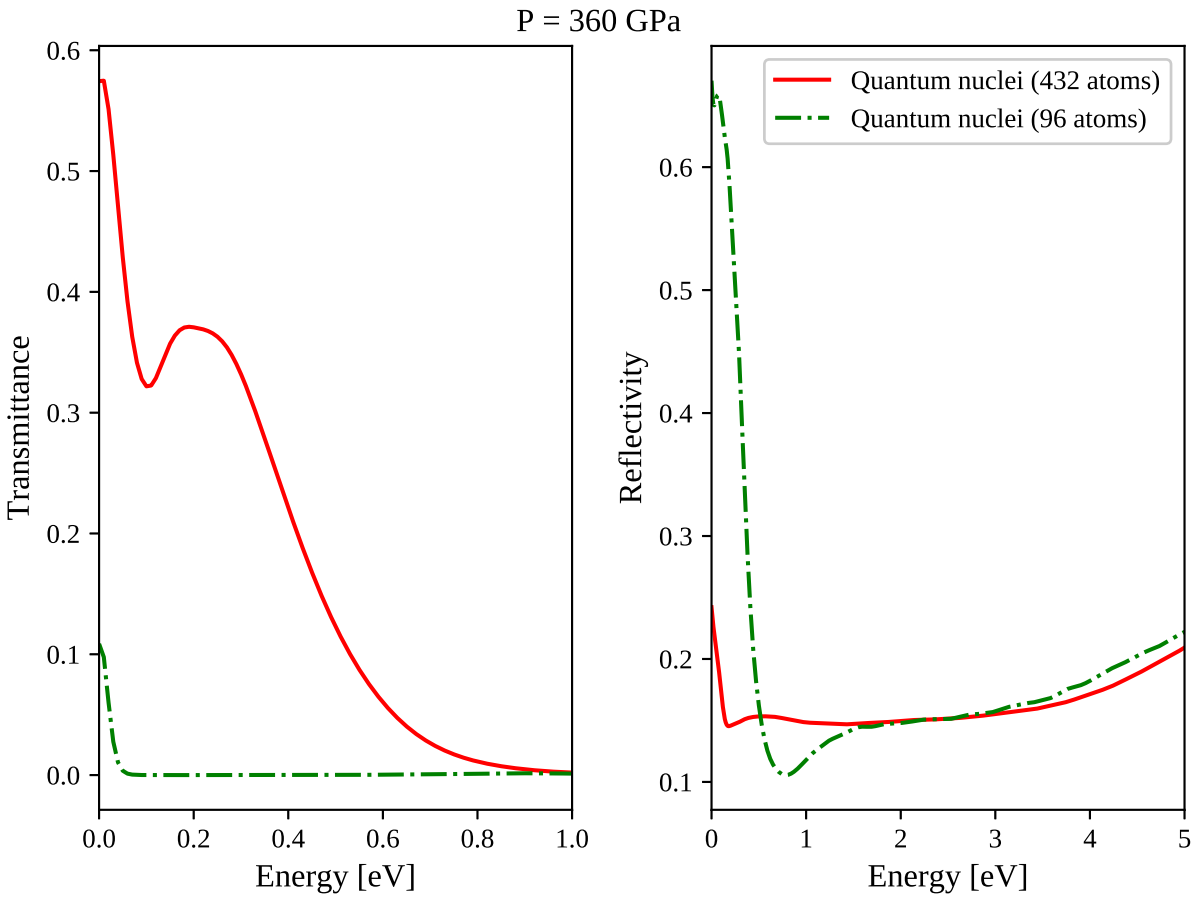

Extended Data Figure 2. Comparison of the optical properties with two different simulation cells, containing 96 and 432 atoms respectively. Also, in this case, the optical gap is completely missed by using a small simulation cell. This effect is due to the combination of the overestimation of the Drude peak in the small cell that results from the higher DOS close on the Fermi level (see Extended Data Figure 1) and a subsequent increment of the plasma frequency and the reflectivity at low energy that kills the absorption profile. Moreover, the optical gap is also strongly affected by optical transitions involving phonons with q points not commensurate with the cell of 96 atoms. These simulations are performed using the BLYP functional using the structures at 355 GPa.

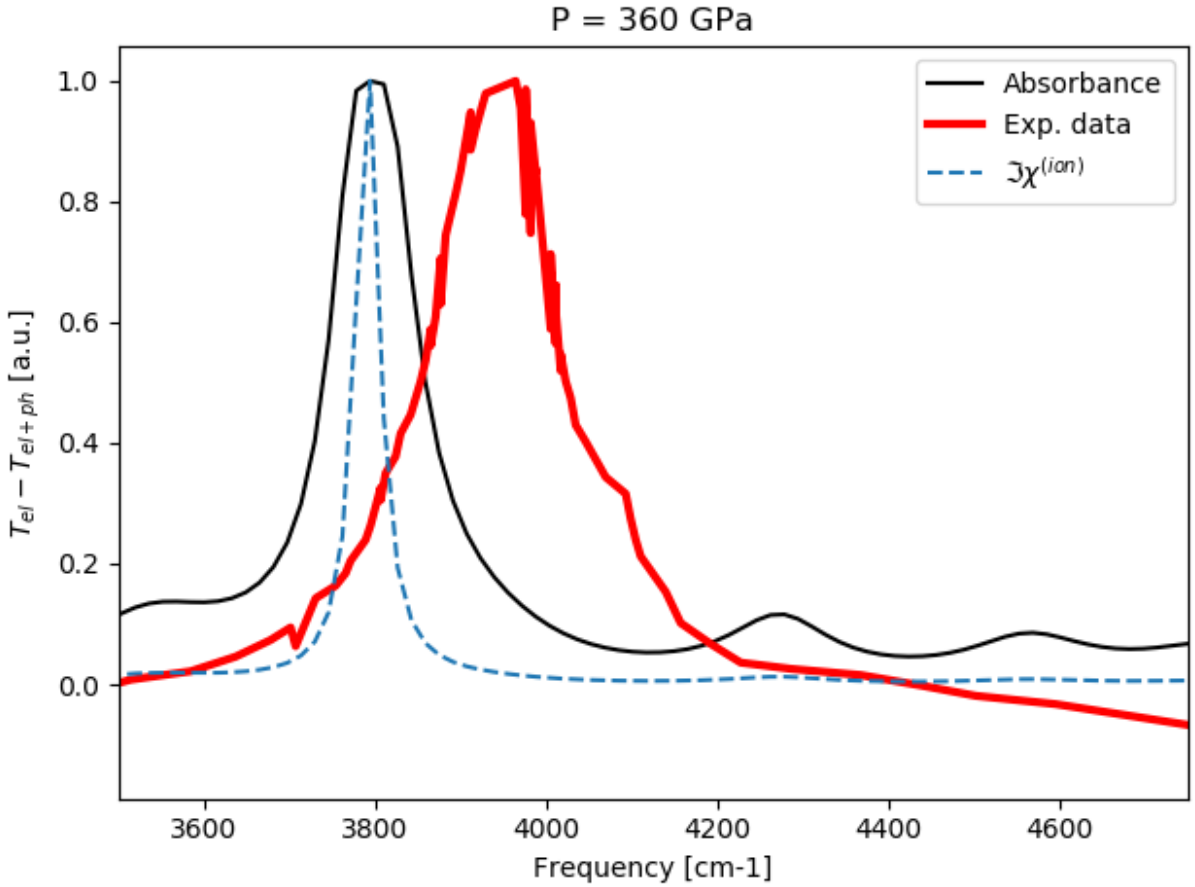

Extended Data Figure 3. The IR vibron at 355 GPa computed as the absorbance and the imaginary part of the ionic green function only. The IR vibron linewidth cannot be explained by anharmonicity alone, but requires properly accounting for the absorbance induced by the negative dielectric function between the TO mode (the pole of the susceptibility) and the LO one (induced by the effective charges)

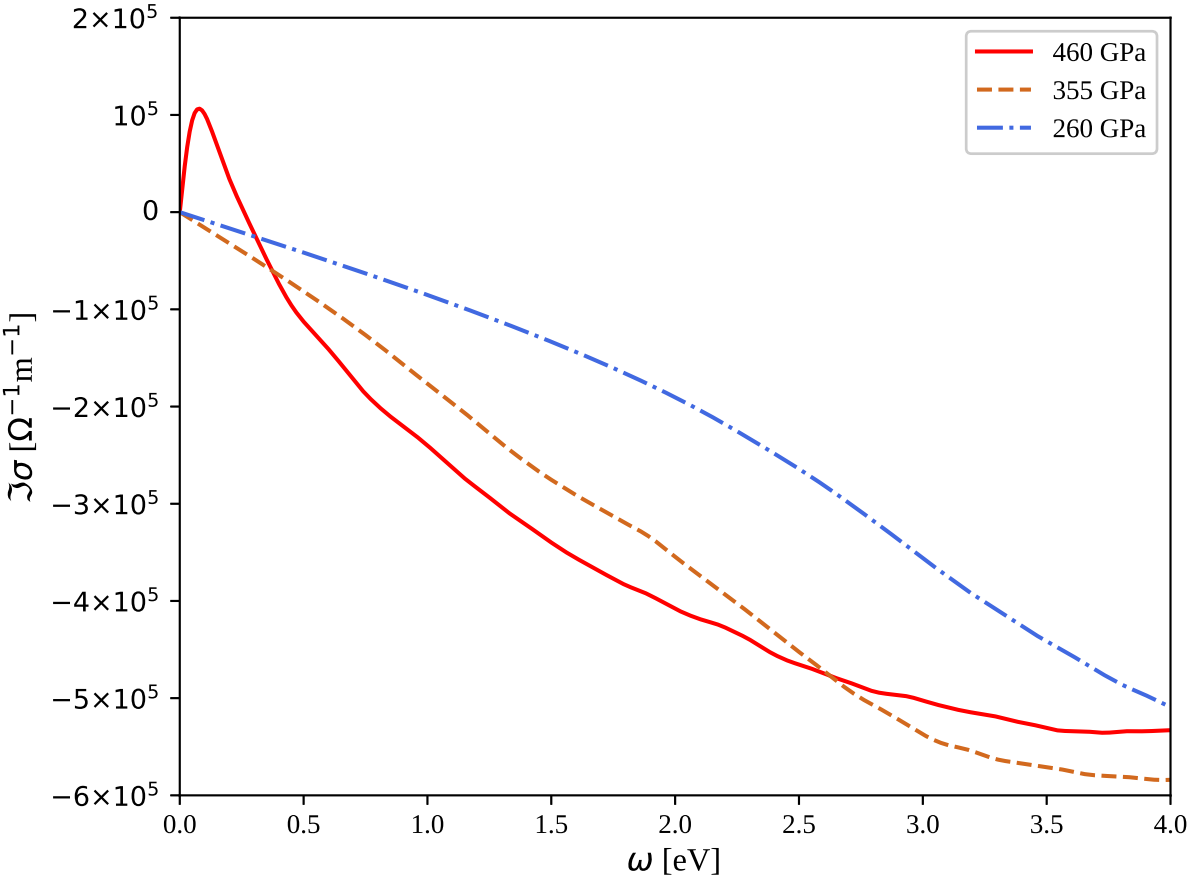

Extended Data Figure 4. Imaginary part of the conductivity at the simulated pressures. Combining these data with the real part if the conductivity reported in Extended Data Figure 4 of the main text, it is possible to compute the dielectric function and the all the optical properties (reflectivity and transmittance). These data are computed with quantum nuclei using the TB09 functional.

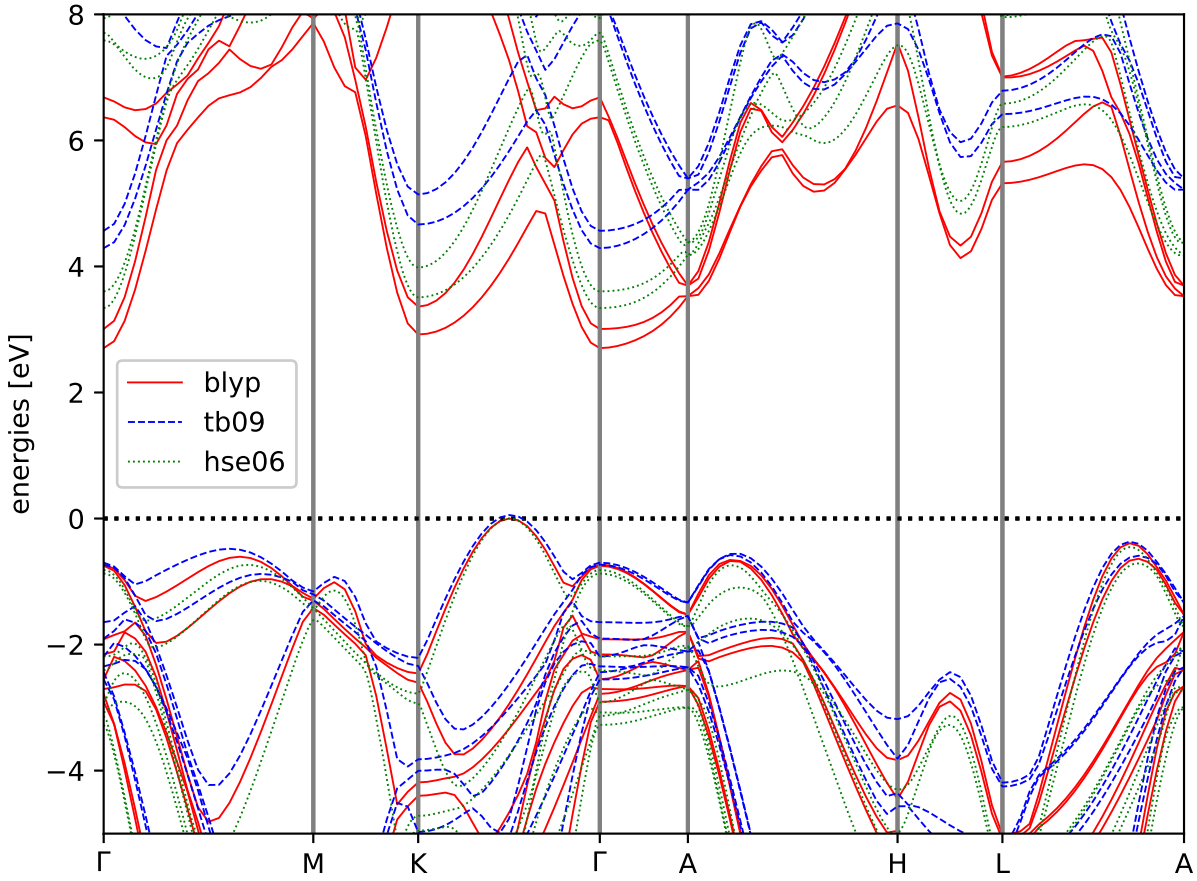

Extended Data Figure 5. Comparison of the band structure at 260 GPa for the average centroid position with different DFT exchange-correlation functionals. TB09 is the functional we used for computing optical properties in the main text. Since the structure is very close to a hexagonal cell, we adopt the typical k-path along high symmetry lines for hexagonal crystals. Both HSE06 and TB09 go beyond DFT, employing, respectively, hybrid and meta-GGA functionals. HSE06 is a general-purpose functional that provide very good electronic bands, at a much high computational cost required by the calculation of the exact exchange. On the other side, TB09 is aimed only to compute electronic properties, present a lot of limitations on isolated atoms, but it has a computational cost comparable to that one of BLYP (allowing calculation with more atoms in the cell). The precision of TB09 and HSE06 in the band structure calculation is comparable. By assuming a similar accuracy of TB09 and HSE06[1] we can estimate an error of 0.4 eV in the band-gap of each functional on static configurations.

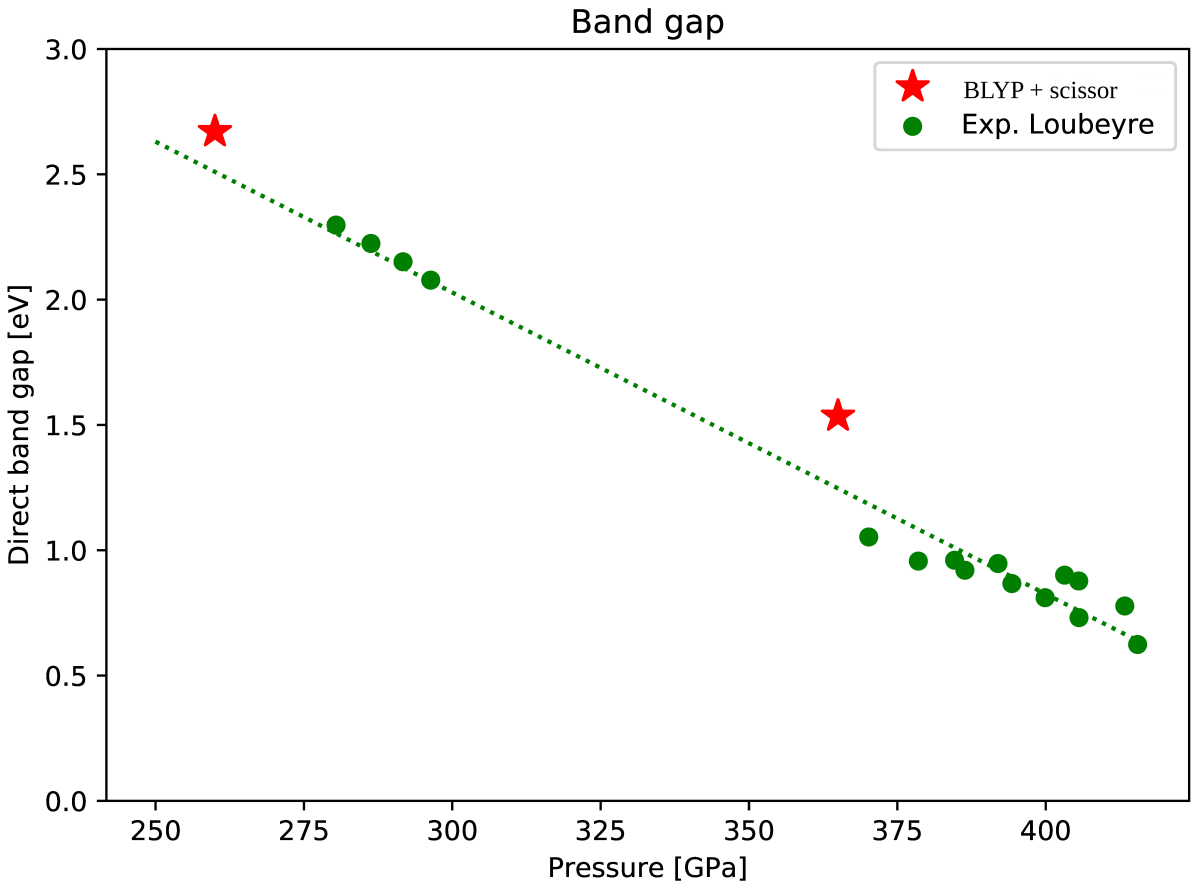

Extended Data Figure 6. The direct gap with quantum fluctuations estimated with the BLYP functional plus a constant scissor correction as discussed in[2], to match the value of the QMC results. As clearly shown, the difference with the results reported by using TB09 (main text, figure 3 panel d) provides an estimation of the error on the band-gap due to the exchange-correlation functional of about 0.3 eV. This is a bit lower than what we obtained by comparing TB09 and HSE06 on a static snapshot in Extended Data Figure 5. This probably indicates that the choice of the DFT functional for the band gap is less sensitive in the ionic displaced configurations than in the static ones.

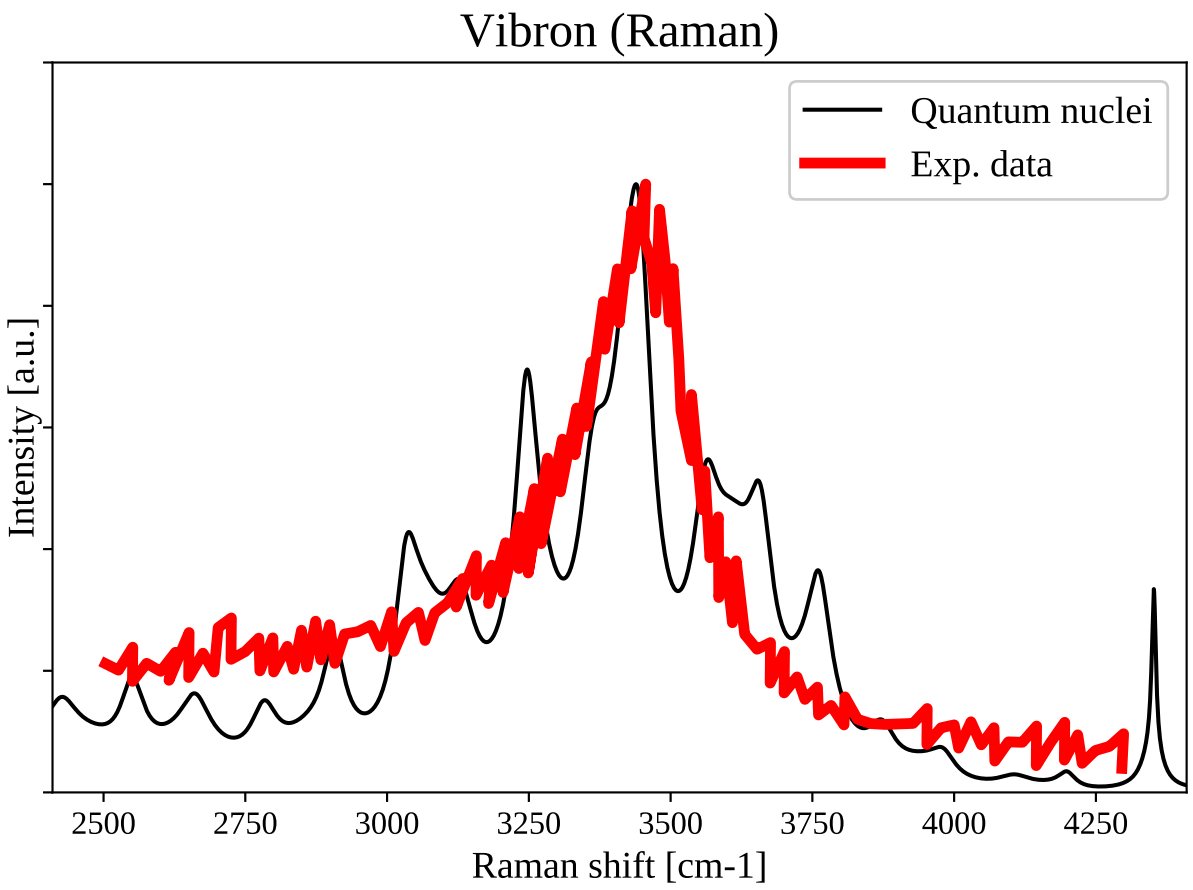

Extended Data Figure 7. Comparison between the Raman spectrum at 360 GPa computed with quantum nuclei (anharmonic) and experimental data. The simulated spectrum has been shifted to match the vibron energy of experiments to compare the lineshape.

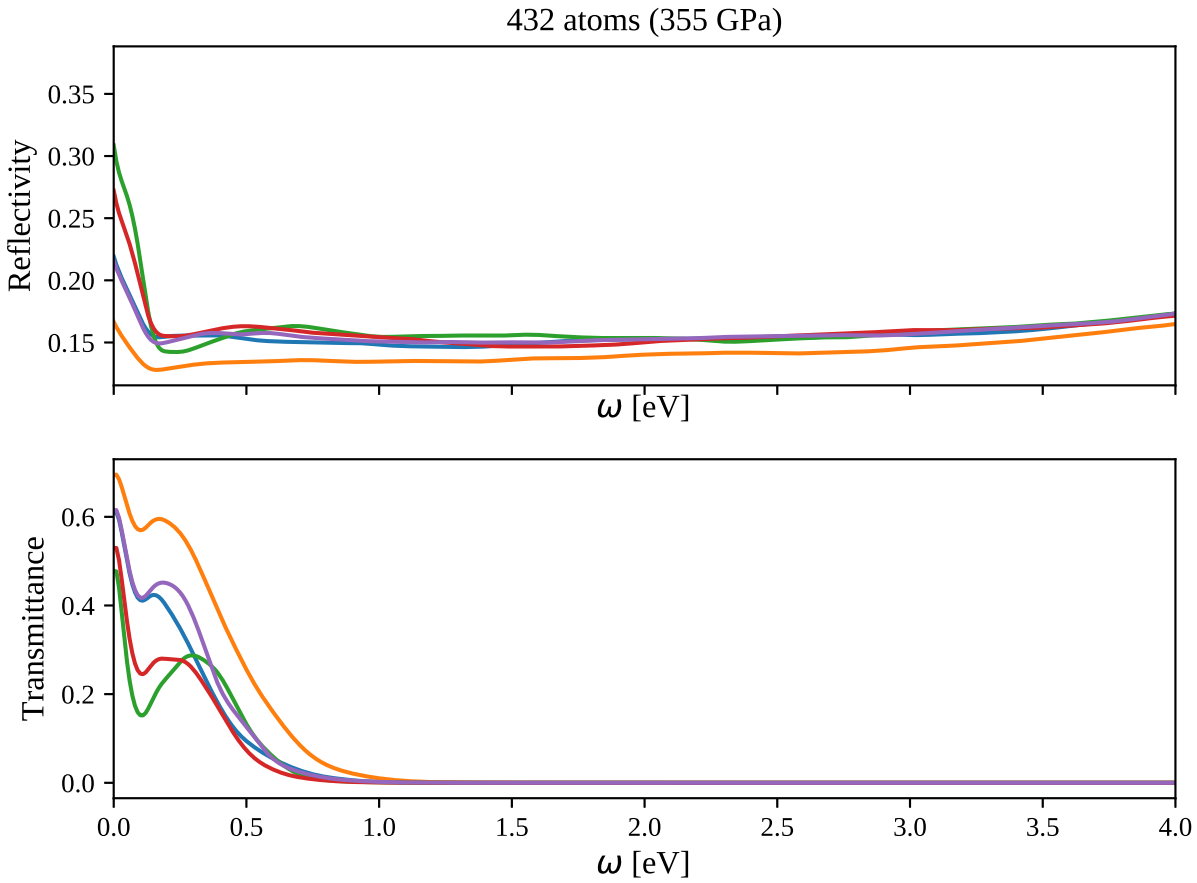

Extended Data Figure 8. Comparison between reflectivity and transmittance obtained with different configurations extracted by the nuclear density matrix with 432 atoms. The stochastic error for each configuration on the gap is about 0.1 eV

Pressure				
155 GPa	90	90.0779	90	$\widehat{BC}, \widehat{AC}, \widehat{AB}$
	3.14545	5.44694	5.65907	A, B, C
	0.08567	0.42309	0.37493	H
	-0.28381	0.02837	0.37506	H
	-0.31564	0.29502	0.38737	H
	-0.41136	0.41238	0.37962	H
	0.10180	0.17811	0.36305	H
	0.32473	0.16163	0.37004	H
260 GPa	90	90.1981	90	$\widehat{BC}, \widehat{AC}, \widehat{AB}$
	2.93362	5.07765	5.23661	A, B, C
	0.07224	0.41153	0.37507	H
	-0.28350	0.02592	0.37457	H
	-0.31687	0.29765	0.39083	H
	-0.42629	0.42424	0.37910	H
	0.10805	0.17792	0.35891	H
	0.35134	0.16296	0.37160	H

(a)

Pressure				
355 GPa	90	90.1665	90	$\widehat{BC}, \widehat{AC}, \widehat{AB}$
	2.80707	4.85289	4.99180	A, B, C
	0.06582	0.40343	0.37493	H
	-0.28505	0.02670	0.37442	H
	-0.31753	0.29794	0.39023	H
	-0.43276	0.43269	0.37835	H
	0.10813	0.17763	0.35940	H
	0.36675	0.16318	0.37255	H
460 GPa	90	90.0255	90	$\widehat{BC}, \widehat{AC}, \widehat{AB}$
	2.69999	4.66242	4.80103	A, B, C
	0.05831	0.39507	0.37462	H
	-0.28856	0.02931	0.37475	H
	-0.31170	0.29847	0.38701	H
	-0.44174	0.44058	0.37721	H
	0.10605	0.17449	0.36245	H
	0.38264	0.16452	0.37395	H

(b)

Extended Data Figure 9. Average nuclear positions of phase III (C2/c symmetry group) after the relaxation with quantum effects, both on the cell and the atoms within the BLYP functional. All the Wyckoff positions are 8f. Only symmetry nonequivalent atoms in crystal coordinates are given. The lattice parameters are given in $\mathring{A}$ and angles in degrees. The structures are in the conventional monoclinic cell. The data in the primitive cell of Fig. 1 in the main text are obtained as $a = \frac{1}{2}\sqrt{A^2 + B^2}$, $c = C$ and $\gamma = 2\arctan(A/B)$

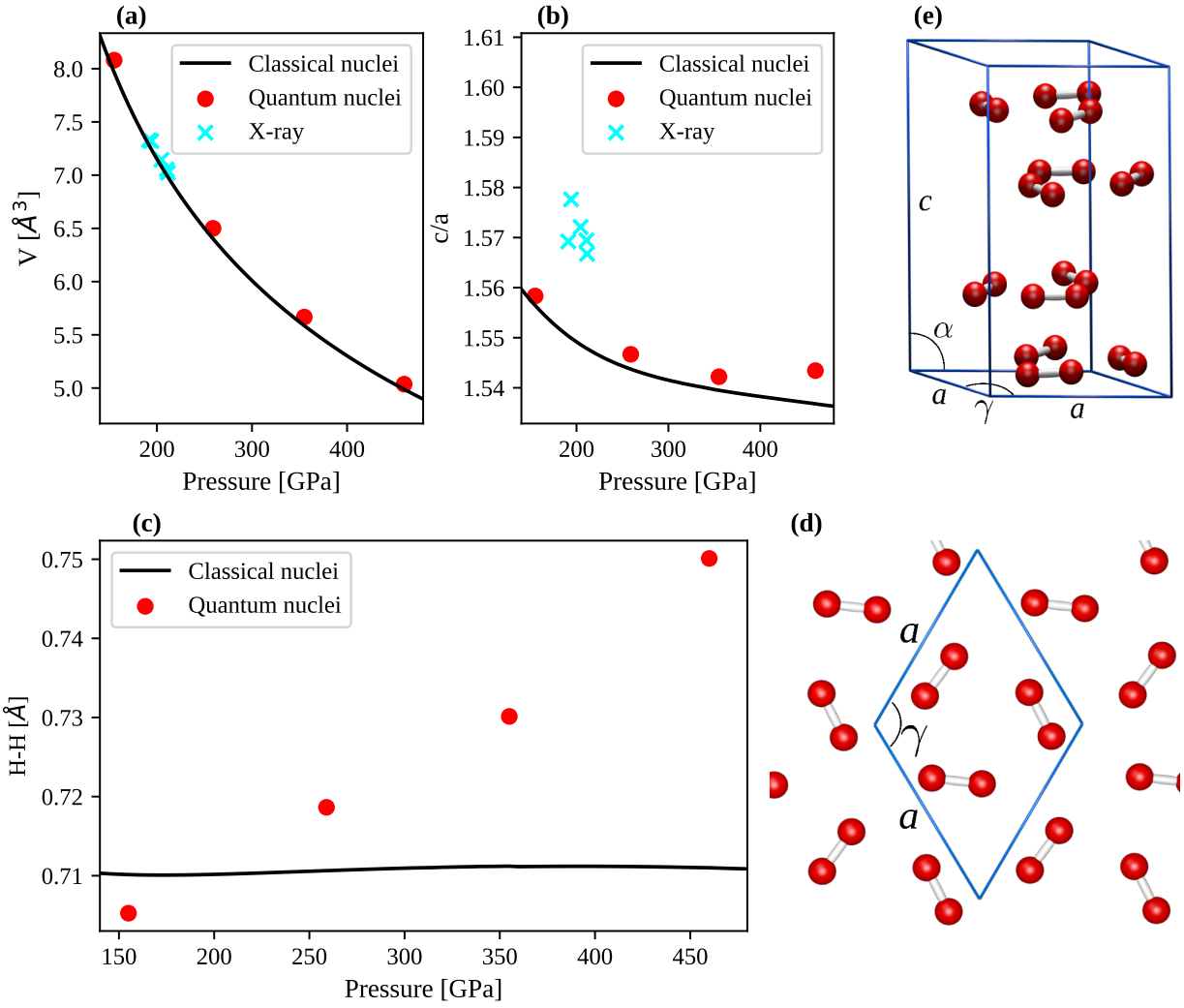

Extended Data Figure 10. Structural data of phase III compared with the X-Ray diffraction experiments computed by[3]. The discrepancies on the c/a ratio is probably due to the different temperature between the simulation (0 K) and the experiment (room temperature). The c and a parameter, as well as the unit cell volume, have been resized to account for the fact that Xray diffraction does not distinguish the single atoms in the molecule, and thus identifies a different cell periodicity. $a' = a/\sqrt{3}$, $c' = c/2$ and $V' = V/6$